 CMES, vol.76, no.4, pp.235-266, 2011

Simulation of Reactive Fluid Flow in a Solid Rocket Motor Combustion-Chamber with/without Nozzle

W. A. El-Askary[1,2], S. A. Wilson[2] and A. Hegab[2]

Abstract: In the present work, a complete simulation of reactive flow in the combustion chamber of a rocket motor equipped with convergent-divergent nozzle has been introduced. The model describes the combustion process inside the combustion chamber considering a steady premixed reactant gas injected through side porous walls of the combustion chamber. The products flow through a convergent-divergent nozzle with adiabatic impermeable walls. The reactants are treated as two-dimensional, multi-components, turbulent compressible flow. The local properties of the mixture are calculated and updated during the solution process. At the boundary of the combustion chamber, a constant mass flux and predefined properties are considered. The proposed model employs the basic conservation equations of continuity, momentum and energy as well as the finite rate of reaction and species transport equations. Finite volume method is used to solve the basic nonlinear partial differential equations numerically.

Preliminary tests are considered including cold as well as combustion models. The results showed fair agreement with other models in the literature; specially the reaction zone depth, temperature contours and species concentration along the entire space of the combustion chamber.

Keywords: Solid Propellant; Sandwich Propellant; Diffusion and Premixed Flames; Convergent-Divergent Nozzle; Reactive Flow in Rockets.

1 Introduction

Combustion process plays an important role in governing the gas flow inside the combustion chamber of solid rocket motor (SRM) which in turn controls the overall performance. The mixing process and reaction rate of the fuel and oxidizer

[1] Corresponding author, Tel.: +2-00105255817; Fax: +2-048-2235695, *Email address*: wageeh_elaskary@yahoo.com

[2] Mechanical Power Engineering Department, Faculty of Engineering, Menoufiya University, Shebin El-Kom, Egypt

exhibit clear effect on some important phenomena like combustion instabilities and acoustic waves generated and traveled along the combustion chamber. Many investigators [Tseng, Tseng, Chu and Yang (1994), Chu and Yang (1996), Westbrook and Dryer (1981) and Vyas, Majdalani and Yang (2003)] tried to emulate the solid fuel combustion by using paraffin hydrocarbons fuel as methane CH4 and propane C3H8, while the air is used as oxidizer. Two different fuel/oxidizer configurations may be used in SRM. The first one depends on mixing of the fuel powder with the oxidizer grains at specified equivalence ratio. This method gives premixed flame which is characterized by fast reaction rate, high peak temperature and more uniform temperature gradient inside the combustion chamber. In second configuration, the fuel and oxidizer blocks arrange side by side in a manner that each fuel block is surrounded by two oxidizer blocks as a sandwich. The combustion occurs at the interface surface between the fuel and oxidizer. This arrangement gives diffusion flame which is characterized by relatively slower reaction rate, deeper flame zone and non regular surface topography of the solid reactants. Another important trial to simulate integral rocker ram-jet (IRR) is presented by Cherng , Yang and Kuo (1989). In their work, they introduced a mathematical model to simulate the turbulent diffusion combustion in IRR propulsion system. They indicated the importance of the design parameters on the propulsion efficiency.

In present work, a comprehensive code (cold as well as combustion model) is developed to simulate the combustion process and gas flow inside the combustion chamber of the solid rocket. The code is capable to simulate the combustion process at different combustion modes (premixed, diffusion) and different flow regimes (laminar and turbulent). The cold model is validated against the experimental data of Mason, Putnom and Re (1980), while the combustion model is validated by comparing its results with other published data [Tseng, Tseng, Chu and Yang (1994) and Chu and Yang (1996)].

2 Mathematical model

In the present work a mathematical model for simulating the combustion process in SRM combustion chamber is introduced. The model is based on employing the strongly coupled set of nonlinear partial differential equations representing the conservation equations of mass and momentum in addition to a suitable turbulence model to compute the turbulence viscosity. The energy equation and the transport of species along the combustion chamber are also included. The cold model first addresses the effect of injected mass flux on the generation and location of the shock wave. The combustion model is used to address the effect of combustion mode on the flow pattern inside the combustion chamber, so both premixed and diffusion combustion are modeled. The flow is treated as two-dimensional,

compressible (laminar or turbulent) at steady state conditions. The mathematical representation of the model is summarized in the following subsections.

Continuity equation:

$$\frac{\partial \rho}{\partial t} + \frac{\partial \rho u_i}{\partial x_i} = 0.0 \tag{1}$$

Momentum equation:

$$\frac{\partial \rho u_i}{\partial t} + \frac{\partial \rho u_i u_j}{\partial x_j} = -\frac{\partial p}{\partial x_i} + \frac{\partial}{\partial x_j}\left(\mu_{eff}\left(\frac{\partial u_i}{\partial x_j} + \frac{\partial u_j}{\partial x_i} - \frac{2}{3}\delta_{ij}\frac{\partial u_k}{\partial x_k}\right)\right) \tag{2}$$

where, u_i and u_j are the streamwise ($i-$direction) velocity and the normal to main flow ($j-$direction) velocity, respectively. δ_{ij} is the Kronecker's delta function (δ_{ij}=1 if $i = j$ and δ_{ij}=0 if $i \neq j$). The effective viscosity is obtained from: $\mu_{eff} = \mu_\ell + \mu_t$; where μ_ℓ is the laminar viscosity and μ_t is the turbulent viscosity, which needs a suitable turbulence model.

Turbulence modeling:

The modified version of $v^2 - f$ model of Lien and Kalitzen (2001) and successfully recently used by El-Askary, Balabel, El-Behery and Hegab (2010) will be considered here. The distinguishing feature of the $v^2 - f$ model is its use of the velocity scale,v^2 instead of the turbulent kinetic energy, k, for evaluating the eddy viscosity. The velocity scale v^2, which can be thought of as the velocity fluctuation normal to the streamlines, has shown to provide the right scaling in representing the damping of turbulent transport close to the wall, a feature that k does not provide.

The distribution of the turbulent viscosity is calculated from:

$$\mu_t = \rho C_\mu v^2 Time \tag{3}$$

where *Time* is the turbulent time scale and is given by:

$$Time = \max[\frac{k}{\varepsilon}, 6\sqrt{\frac{\mu}{\rho\varepsilon}}] \tag{4}$$

The standard $k - \varepsilon$ equations read

$$\frac{\partial}{\partial x_j}(\rho u_j k) = \frac{\partial}{\partial x_j}\left[(\mu + \frac{\mu_t}{\sigma_k})\frac{\partial k}{\partial x_j}\right] + \rho(P_r - \varepsilon) \tag{5}$$

$$\frac{\partial}{\partial x_j}(\rho u_j \varepsilon) = \frac{\partial}{\partial x_j}\left[(\mu + \frac{\mu_t}{\sigma_\varepsilon})\frac{\partial \varepsilon}{\partial x_j}\right] + \frac{\rho}{Time}(C_{1\varepsilon}P_r - C_{2\varepsilon}\varepsilon) \tag{6}$$

where P_r and ε represent the production rate and the dissipation rate of the turbulent kinetic energy, k, respectively; while σ_k and σ_ε are model constants. The production rate is related to the mean strain of the velocity field through the Boussinesq assumption. That is;

$$P_r = \mu_t S^2 \tag{7}$$

where S is defined as:

$$S = \sqrt{\frac{1}{\rho}\left(\frac{\partial u_j}{\partial x_i} + \frac{\partial u_i}{\partial x_j} - \frac{2}{3}\delta_{ij}\frac{\partial u_k}{\partial x_k}\right)\frac{\partial u_i}{\partial x_j}} \tag{8}$$

The v^2 transport equation can be expressed as:

$$\frac{\partial}{\partial x_j}(\rho u_j v^2) = \frac{\partial}{\partial x_j}\left[(\mu + \frac{\mu_t}{\sigma_k})\frac{\partial v^2}{\partial x_j}\right] + \rho(kf - 6v^2\frac{\varepsilon}{k}) \tag{9}$$

and the elliptic-relaxation equation f can be represented as:

$$L^2\frac{\partial^2 f}{\partial x_j^2} - f = \frac{1}{T}\left[(C_1 - 6)\frac{v^2}{k} - \frac{2}{3}(C_1 - 1)\right] - C_2\frac{P_r}{k} \tag{10}$$

The turbulent length scale L is determined from the values of k and ε as follows:

$$L = C_L \max[\frac{k^{3/2}}{\varepsilon}, C_\eta\frac{(\mu/\rho)^{3/4}}{\varepsilon^{1/4}}] \tag{11}$$

The constants of the model are given as follows; see El-Askary, Balabel, El-Behery and Hegab (2010):

$$\begin{aligned} &C_\mu = 0.22; \quad \sigma_k = 1; \quad \sigma_\varepsilon = 1.3; \quad C_{1\varepsilon} = 1.4(1 + 0.05\sqrt{k/v^2}); \\ &C_{2\varepsilon} = 1.9; \quad C_1 = 1.4; \quad C_2 = 0.3; \quad C_L = 0.23; \quad C_\eta = 70. \end{aligned} \tag{12}$$

As noticed, all model constants are completely wall-distance independent (El-Askary, Balabel, El-Behery and Hegab (2010)).

Energy equation:

$$\frac{\partial}{\partial t}\left(\rho\left(h + \frac{1}{2}V^2 - \frac{p}{\rho}\right)\right) + \frac{\partial}{\partial x_i}\left[\rho u_i\left(h + \frac{1}{2}V^2\right)\right] = \frac{\partial}{\partial x_j}\left[k_{eff}\frac{\partial T}{\partial x_j} + u_i(\tau_{ij})_{eff}\right] + S_R \tag{13}$$

where, k_{eff} is the effective thermal conductivity, S_R is the energy source term and will be discussed later and $(\tau_{ij})_{eff}$ is the effective stress tensor. The enthalpy of gas h is computed from:

$$h = \sum_{i=1}^{N} Y_i h_i \tag{14}$$

and the specific enthalpy of species i

$$h_i = \int_{T_{ref}}^{T} C_{pi} dT \tag{15}$$

The effective thermal conductivity is defined as:

$$k_{eff} = k + \frac{C_p \mu_t}{\mathrm{Pr}_t} \tag{16}$$

where, C_p is the specific heat at constant pressure and Pr_t is the turbulent Prandtl number.

Species equation:

The species transport equations for different reactive components can be generally written as:

$$\frac{\partial \rho Y_i}{\partial t} + \frac{\partial \rho u Y_i}{\partial x} + \frac{\partial \rho v Y_i}{\partial y} = \frac{\partial}{\partial x}\left(D_{eff,i}\frac{\partial Y_i}{\partial x}\right) + \frac{\partial}{\partial y}\left(D_{eff,i}\frac{\partial Y_i}{\partial y}\right) + S_i \tag{17}$$

In the above equation Y_i is the local mass fraction of species i, *while* S_i is its source term. These N-species ($N = 5$ in the present study) are the fuel, oxygen, carbon dioxide, water vapor and nitrogen, respectively. To ensure species conservation, only four transport equations are solved, while the fifth species which is nitrogen is calculated as follows:

$$Y_{N_2} = 1 - (Y_f + Y_{O_2} + Y_{CO_2} + Y_{H_2O}) \tag{18}$$

where f denotes to the fuel, which in our case of study represents the methane CH_4 or propane C_3H_8. The effective diffusion coefficient $D_{eff,i}$ can be calculated as follows:

$$D_{eff,i} = \rho D_{im} + \frac{\mu_t}{Sc_t} \tag{19}$$

The first term constitutes the effect of laminar diffusivity, while the second term accounts the effect of turbulence on the diffusion of species with Sc_t as Schmidt number. In laminar flow, this term is vanished.

2.1 Methane Combustion

In the current model validation, single-step kinetic reaction of methane combustion is considered as proposed in Tseng, Tseng, Chu and Yang (1994). The stoichiometric combustion equation is written as follows:

$$CH_4 + 2(O_2 + 3.76N_2) \rightarrow CO_2 + 2H_2O + 7.52N_2 \tag{20}$$

The source term of each species is calculated from the following finite rate equations [Tseng, Tseng, Chu and Yang (1994)].

$$S_{CH_4} = -1.3 \times 10^8 \exp\left(\frac{-E_a}{R_u T}\right) \rho Y_{CH_4}^{-0.3} Y_{O_2}^{1.3} \left(\frac{M_{CH_4}}{M_{O_2}}\right)^{1.3} \tag{21}$$

$$S_{O_2} = 2 \left(\frac{M_{CH_4}}{M_{O_2}}\right) S_{CH_4} \tag{22}$$

$$S_{CO_2} = -1 \left(\frac{M_{CH_4}}{M_{CO_2}}\right) S_{CH_4} \tag{23}$$

$$S_{H_2O} = -2 \left(\frac{M_{CH_4}}{M_{H_2O}}\right) S_{CH_4} \tag{24}$$

The activation energy E_a is 30 k cal/mole [Tseng, Tseng, Chu and Yang (1994)] and R_u is the universal gas constant.

2.2 Propane combustion

The second validation case is based on premixed propane flame in 2D duct [Chu and Yang (1996)]. The stoichiometric single-step combustion is as follows:

$$C_3H_8 + 5(O_2 + 3.76N_2) \rightarrow 3CO_2 + 4H_2O + 18.8N_2 \tag{25}$$

The source term of each species is calculated from the following finite rate equations [Chu and Yang (1996)].

$$S_{C_3H_8} = -4.836 \times 10^9 \exp\left(\frac{-E_a}{R_u T}\right) \rho^{1.75} \left(\frac{Y_{C_3H_8}}{M_{C_3H_8}}\right)^{0.1} \left(\frac{Y_{O_2}}{M_{O_2}}\right)^{1.65} M_{C_3H_8} \tag{26}$$

$$S_{O_2} = 5 \left(\frac{M_{C_3H_8}}{M_{O_2}}\right) S_{C_3H_8} \tag{27}$$

$$S_{CO_2} = -3 \left(\frac{M_{C_3H_8}}{M_{CO_2}}\right) S_{C_3H_8} \tag{28}$$

$$S_{H_2O} = -4 \left(\frac{M_{C_3H_8}}{M_{H_2O}} \right) S_{C_3H_8} \tag{29}$$

The energy source term is calculated by

$$S_R = \sum_{i=1}^{N} S_i h_f^0 \tag{30}$$

Where h_f^0 is the enthalpy of formation at a reference temperature T_{ref}.
The specific heat of gas mixture is calculated as:

$$C_p = \sum_{i=1}^{N} Y_i C_{pi} \tag{31}$$

where

$$C_{pi} = \sum_{j=0}^{4} a_{ji} T^i \tag{32}$$

The coefficients of specific heat polynomial for different species are given in Table 1.

The effect of fluid turbulence on the finite rate of reaction kinetics is considered as described in modified Eddy Breakup model 'EBU' [Srinivasan, Reynolds, Ball, Berry, Johnson and Mongia (1983)], which was proposed originally by Spalding [Spalding (1971) and Spalding (1976)]. In this model the effect of turbulence appears clearly on chemical reaction due to the local vortex stretching. So, the reaction rates S_f in the case of turbulent combustion are calculated as the minimum of rate calculated from Arrhenius law (S_1) and that calculated by EBU model (S_2) as follows:

S_1 =Arrhenius law (Equations 21 and 26)

$$S_2 = C_R \rho \min \left| Y_f, \frac{Y_{O2}}{r_1} \right| \frac{\varepsilon}{k} \tag{33}$$

$$S_f = -\min |S_1, S_2| \tag{34}$$

Where, $C_R = 3$ [Fluent 6.3 (2006)] and $r_1 = (N_{O2}/N_f)(M_{O2}/M_f)$, while N_{O2} and N_f are the number of moles of oxygen and fuel molecules in stoichiometric reaction, respectively.

Equation of State

Table 1: Polynomial coefficients of specific heat [Heywood (1986)]

species	Temperature range (K)	a_0	a_1	a_2	a_3	a_4
$\mathbf{O_2}$	300-5000	811.1803	0.4108345	-0.0001750725	3.757596e-08	-2.973548e-12
$\mathbf{N_2}$	300-5000	938.8992	0.3017911	-8.109228e-05	8.263892e-09	-1.537235e-13
$\mathbf{H_2O}$	300-5000	1609.791	0.740494	-9.129835e-06	-3.813924e-08	4.80227e-12
$\mathbf{CO_2}$	300-1000	429.9289	1.874473	-0.001966485	1.297251e-06	-3.999956e-10
	1000-5000	841.3765	0.5932393	-0.0002415168	4.522728e-08	-3.15313e-12
$\mathbf{C_3H_8}$	300-1000	169.1106	5.032259	0.001024072	-4.008482e-06	1.74279e-09
	1000-5000	1418.847	3.561693	-0.001184807	1.730731e-07	-9.073593e-12
$\mathbf{CH_4}$	300-1000	403.5847	9.057335	-0.01442509	1.580519e-05	-6.343051e-09
	1000-5000	872.4671	5.305473	-0.002008295	3.516646e-07	-2.33391e-11

Finally, the equation of state determines the density distribution of the gas mixture from the pressure, temperature and species mass fraction:

$$P = \rho R_u T \sum_{i=1}^{N} Y_i / M_i \tag{35}$$

where, M_i is the molecular weight of species i.

3 Computational domain and boundary conditions

The cases used in the model validation assume the flow to be steady, 2D compressible and reactive flow. The fuel is considered as gaseous hydrocarbon injected from porous wall perpendicular to the main stream. Two gaseous fuels are considered in the present validation and they are propane and methane. For propane combustion, a channel of length, L of $1m$ and half height, H of 0.05 m is used, as shown in Fig. 1-a. At the lower boundary, a uniform mass flux of 0.21 kg/m^2s of premixed propane-air mixture at a temperature of $350K$ and one atmosphere is injected. While for methane combustion, a channel length of 0.6 m and height of 0.05 m and a uniform mass flux of 0.2 kg/m^2s are used. Seven slots are made in the injection surface each of $20mm$ width for fuel/oxidizer to provide diffusion flame, as shown in Fig. 1-b. The left side of the 2D ducts is closed and no-slip adiabatic wall is considered. The right side is opened to atmosphere at which no gradient in flow parameters exists. While the flow pattern is considered to be symmetrical about the axial direction, only half domain is considered as shown in Fig. 1. For turbulence behavior near the wall, details of the used turbulence model are extensively explained in [El-Askary, Balabel, El-Behery and Hegab (2010)].

4 Numerical treatments

The previously mentioned nonlinear differential equations are solved numerically by using control volume method [Versteeg and Malalasekera (2007)] and the upwind technique as discritization scheme. Demirdzic, Lilek and Peric (1993) presented an extended SIMPLE method that implicitly incorporates the influence of pressure on density for simulating compressible flows, and reduces to its standard form in the incompressible flow limit. This extended SIMPLE algorithm will be considered in the present work to ensure pressure-velocity coupling in compressible fluid.

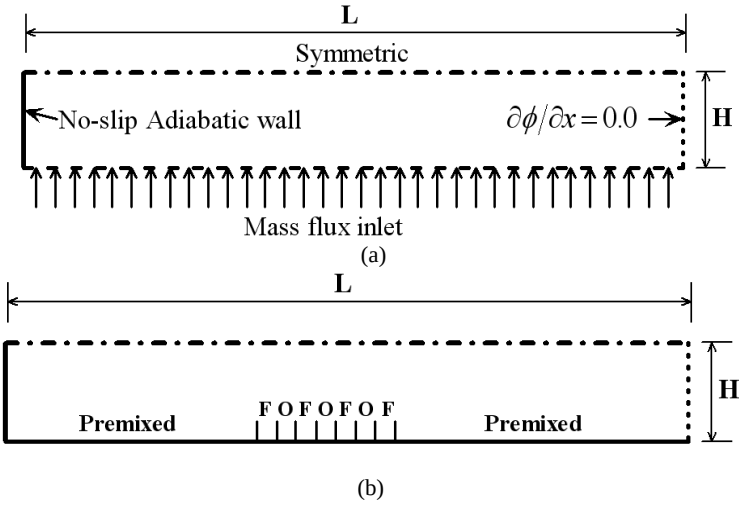

Figure 1: The boundaries in case of premixed combustion of propane in 2D duct (a) and The boundaries in case of methane combustion in dual premixed/diffusion configuration (b)

5 Model validations

5.1 Cold model validation

The preliminary validation considered in the present study is a cold model one, in which a symmetrical two-dimensional duct ended with a convergent-divergent nozzle. The test nozzle used in the present paper is a subscale, two-dimensional convergent-divergent nozzle installed at the end of a chamber of length L=48 cm and half height H/2=10 cm. The flow is generated due to a side-wall injection in the chamber and allowed to develop along the chamber before entering the nozzle, which freely discharges it to atmosphere. The nozzle has a throat area ratio$A_t/A_i = 0.7$, where A_t is the throat area and A_i is the duct cross-section area and an expansion ratio $A_e/A_t = 2.653$, where A_e is the exit area of the nozzle. The convergence and divergence lengths read $1.857cm$ and $1.1196cm$, respectively. The chamber is numerically equipped with different injected mass fluxes from low to high values as: 3.5, 6, 7, 13, 23, 30, 37 and $45(kg/\sec)/m^2$in order to control the shock generation and location inside and behind the nozzle. Schematic representations of the computational domain including a sufficient downstream length of 60 cm after the nozzle exit and the boundaries are sown in Fig. 2.

The successful results previously obtained by El-Askary, Balabel, El-Behery and

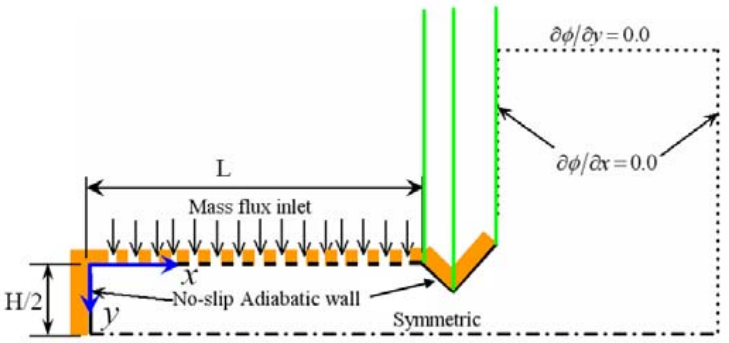

Figure 2: Computational Domain a Rocket Chamber Model Ended with a Convergent-Divergent Nozzle

Hegab (2010) encouraged the present authors to use their developed numerical code including $v^2 - f$ as a turbulence model, because of its simple form with good predicted results. A detailed description and discussion on the governing equations, numerical method and boundary conditions can be found in El-Askary, Balabel, El-Behery and Hegab (2010).

The computational grid covers 296 and 250 in streamwise and vertical directions, respectively. The chamber has 131×81 and there are 23 grid points along the streamwise direction of the convergent part of the nozzle, while 91 grid points are considered in the divergent part. At the exit of the nozzle the vertical direction contains 150 grid points. After the nozzle exit the grid is allowed to expand in the two directions of computational domain. A (not to scale) view of the grid topology used inside the nozzle is shown in Fig. 3 indicating the near-wall velocity V_p and the generated wall-shear stress τ_w. The grid used is generated and considered after different tests including rougher and smoother grids.

Wall Function

In the present work, the flow field in the main flow region is of principle concern. To avoid excessive grid points in the laminar sublayer and the need for detailed calculations in the near wall regions, equations are introduced to link the values of the dependent variables on the wall to those in the logarithmic region. The first grid point in the flow next to the wall is placed just outside the viscous sublayer. At that point, the resulting velocity V_p, parallel to the wall is calculated from the wall function corresponding to the equation for u-velocity, which is given by the

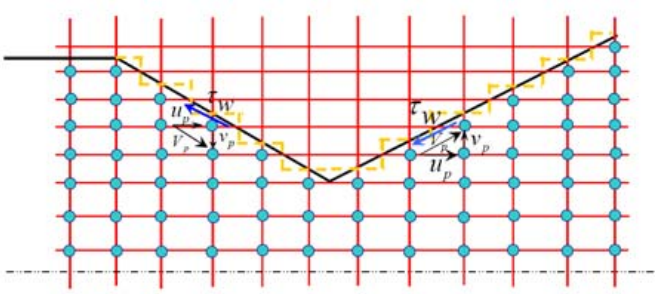

Figure 3: Strategy of the Computational Grid in the Nozzle Domain (not to scale)

log-law equation (see Fig. 3):

$$u^+ = \frac{V_p}{u_\tau} = \frac{1}{\chi}\ln(Ey_p^+) \tag{36}$$

Where, u_τ and y_p^+ are the friction velocity and the dimensionless wall distance defined respectively by:

$$u_\tau = \sqrt{\frac{\tau_w}{\rho_w}}, \quad y_p^+ = \frac{\rho y_p u_\tau}{\mu} \tag{37}$$

τ_w is the total wall shear stress, χ and E are the von-Karman's constant and the roughness parameter, respectively, which have the values of 0.4172 and 9.793, respectively. The log-law equation is applied in the range of non-dimensional wall distance $30 \leq y^+ \leq 200$, where the first grid point (P) must be located. This range lies between the viscous layer and the turbulent outer layer. In this range, local equilibrium prevails. Under this condition, the production of turbulence kinetic energy equals to the turbulence dissipation rate.

5.1.1 Preliminary results

In this section, computational results will be presented in terms of the axial distributions of pressure and Mach number. Normalized computational centerline static pressures (P/P_o), where P_o is the stagnation pressure in the upstream chamber, are presented in Figure 4, plotted against non-dimensional streamwise location at different injection mass fluxes. For the lower mass fluxes 3.5 and $6(kg/\sec)/m^2$, it is observed that the flow is totally subsonic flow, see also Figure 5, where the centerline Mach number is also represented. With increasing the injection mass flux

a supersonic flow starts to appear inside the nozzle but with different flow behavior depending on the injection mass flux. For injection mass flux $7(kg/\sec)/m^2$, a strong normal shock wave clearly appears inside the nozzle, see Figures 4-b and 5-b. With much more increase of the injected mass flux to the value $13(kg/\sec)/m^2$, the shock will be moved towards the nozzle exit and here one can find either a normal shock or Mach dish (a combination of oblique shock near the wall and normal shock in the core) at the exit. The latter is clearly visible form the Mach number distribution, in which the flow returns from subsonic to supersonic again after the shock. By continuous increase of the injection mass flux, the mach dish changes to a Mach cone (intersected oblique shock waves) and the cone length increases with increasing the injected mass. That shows a weaker generated shock in the downstream of the nozzle with the highest injected mass flux.

5.1.2 Validation

In the following, results are presented for a planar nozzle experimentally reported by Mason, Putnam and Re (1980) (Case B-1). The geometrical details for this test case are given in the shown Fig. 6. Computations have been performed using both laminar and turbulent Navier-stokes equations with the present developed code. Also, the Fluent-code results are included to indicate the quality of the present code. The pressure distributions at the wall and centerline are compared with the experimental data of Mason, Putnam and Re (1980), which were taken on the centerline of the end walls.

The numerical grid for the shown half nozzle with an upstream straight duct length of 18 cm and downstream plenum of length 21 cm using a grid of 186×143. The grid spacing was uniform in the transverse direction. In the axial direction, however, more grid points were packed near the throat. The inlet Mach number was taken as 0.232 and the ratio of the exit static pressure to the upstream stagnation pressure was fixed at 0.1135, corresponding to the design condition.

Figure 7 shows the numerical results (using laminar as well turbulent simulations) compared with the experimental data on the centerline and the wall of the nozzle. The local pressure is non-dimensioned using the stagnation pressure at the inlet, while the streamwise length using the total nozzle length. The computational results (wall pressure distribution) using Fluent package (with the same grid resolution) are also implemented. The agreement between the numerical results extracted from the present developed code using the turbulent flow solution and the experimental data is clearly seen to be good at both the nozzle wall and centerline, especially near the throat of the nozzle. The pressure jump noticed near the end of the nozzle may be due to a generated inclined weak shock near the exit of the nozzle. In fact, this has not been clearly measured in the experiment of Mason,

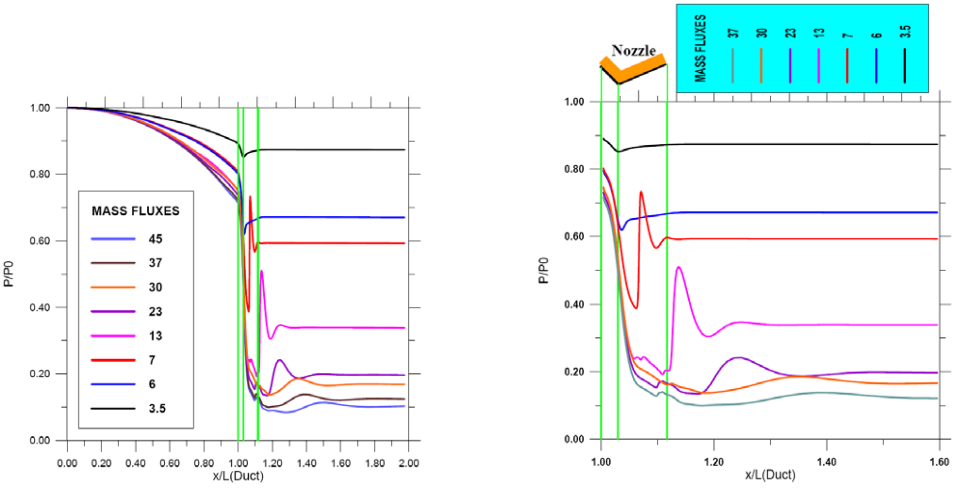

Figure 4: Non-dimensional pressure distributions along the centerline of the entire domain (a) and only the nozzle and the downstream domain (b)

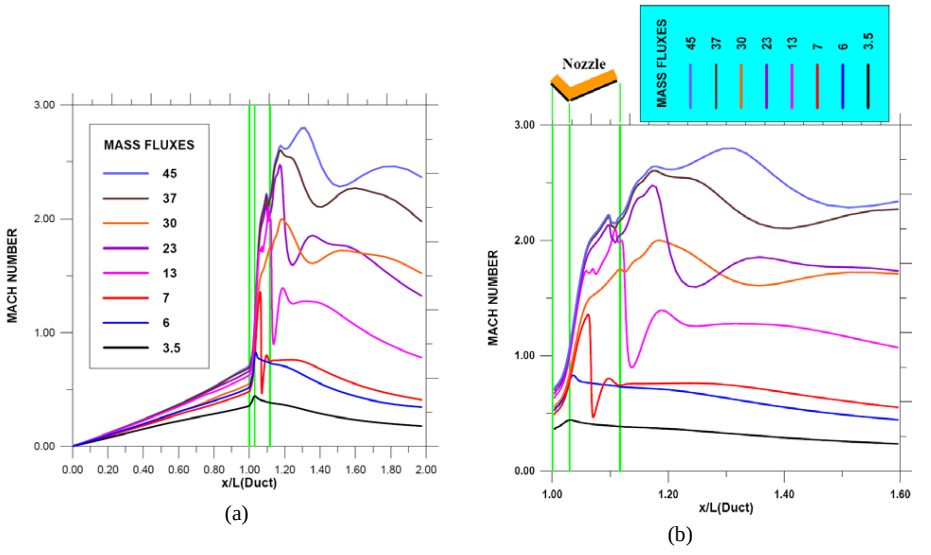

Figure 5: Mach number distributions along the centerline of the entire domain (a) and only the nozzle and the downstream domain (b)

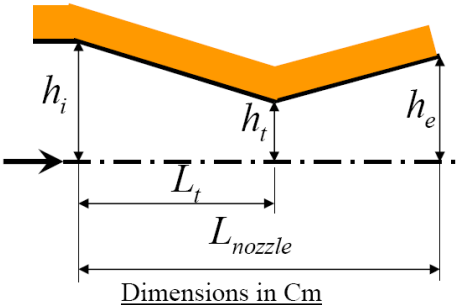

Dimensions in Cm

$$L_{nozzle} = 11.56,\ L_t = 5.78,\ h_i = 3.52,\ h_t = 1.37,\ h_e = 2.46$$

Figure 6: Dimensions of the planar converging-diverging nozzle experimentally considered by Mason, Putnam and Re (1980)

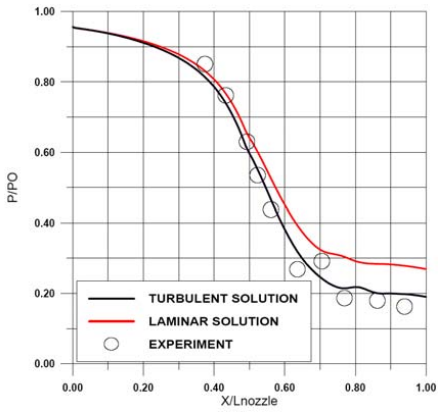

(a)

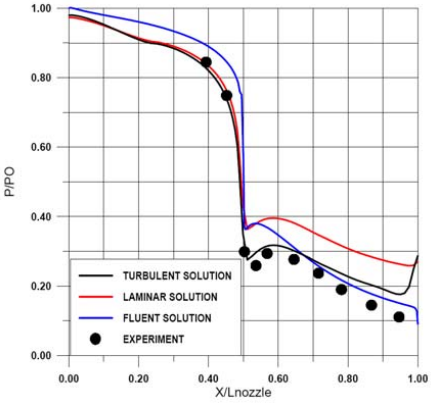

(b)

Figure 7: Pressure distribution along the centerline of the nozzle (a) and along the wall of the nozzle (b); (Symbols: experiments of Mason, Putnam and Re (1980))

Putnam and Re (1980), because of the insufficient measurements resolution near the nozzle exit and not be predicted using Fluent package. Generally as noticed, the best results are obtained from the present simulation of turbulent flow.

5.2 Combustion model

In order to validate the model with comustion, comparisons with other investigators are carried out. Two cases are considered in the present validation. The first case represents the premixed combustion of propane which injected through porous wall

along the entire lower boundary as in Tseng, Tseng, Chu and Yang (1994). Figure 8 shows the rate of fuel and oxygen consumption inside the reaction zone. Up to 1 mm most of fuel is consumed and the products are fixed at the stoichiometric ratio. This behavior appears clearly in the flame temperature as shown in Fig. 9, where the flame temperature attains its maximum value at the end of the reaction zone. Comparing the results of the present model with that of Tseng, Tseng, Chu and Yang (1994) and the output of standard FLUENT code V6.3 [Fluent 6.3 (2006)], the figure shows good agreement between the results of the present model with these of FLUENT code as shown in Fig. 9. Both models use the same numerical method (control volume method), while Tseng, Tseng, Chu and Yang (1994) used the finite different method with pseudo pressure technique to eliminate the probability of singularity. Another comparison with analytical form proposed by Vyas, Majdalani and Yang (2003) appears fair agreement in predicting the maximum temperature as shown in Fig. 10, in spite of clear slower reaction rate is observed in the analytical form output. This behavior can be attributed to the assumption used in deducing the analytical form which states that the heat release from the exothermic reaction is represented statistically by Gaussian distribution and error function. Moreover, neglecting the axial velocity inside the reaction zone, increases the vertical gas momentum and consequently increase the flame zone as shown in Fig. 10. The analytical form is represented as follows [Vyas, Majdalani and Yang (2003)]:

$$T(y) = T_w + \frac{2C_1\sqrt{C_3}y + C_2\sqrt{\pi}}{2\sqrt{C_3}\rho v.\bar{C}_p}\left\{erf\left(C_4\sqrt{C_3}\right) + erf\left[(y - C_4)\sqrt{C_3}\right]\right\} \tag{38}$$

Where, $C_1 = 6.34 \times 10^6$, $C_2 = 1.061 \times 10^9$, $C_3 = 22 \times 10^6$ and $C_4 = 93.251 \times 10^{-5}$. The specific heat for reactant mixture is calculated as follows.

$$C_p(T) = \sum Y_i C_{pi} = Y_{C_3H_8} C_{p.C_3H_8} + Y_{O_2} C_{p.O_2} + Y_{N_2} C_{p.N_2} \tag{39}$$

Where, Y_i is the mass fraction of species$i$, and the average specific heat of reactants can be written as follows:

$$\bar{C}_p = \frac{1}{T_f - T_w}\int_{T_w}^{T_f} C_p.dt \tag{40}$$

with T_w showing the wall temperature.

The second validation test case was established by Chu and Yang (1996). Their computational domain was described previously as shown in Fig. 1 (b). It consists of three different gas injection configurations from the porous side walls. The first

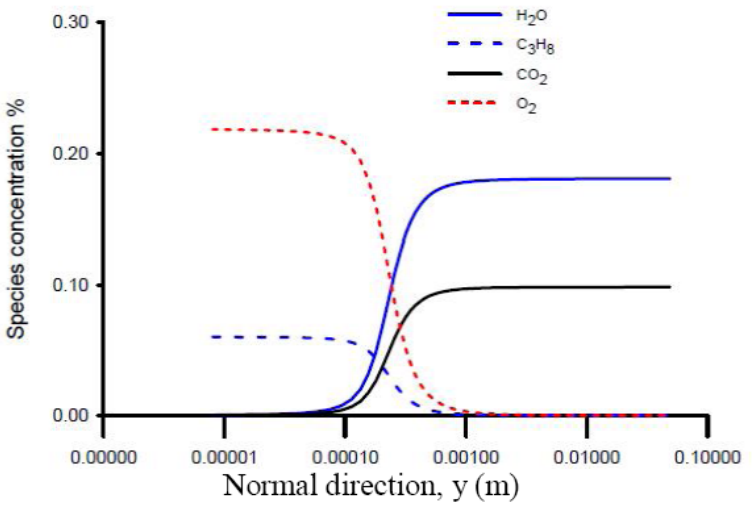

Figure 8: Species concentration of premixed propane combustion at normal direction

and the third are premixed combustible mixture. While at the middle is a series of consecutive fuel and oxidizer slots, 20 *mm* width each and arranged in sandwich type to produce diffusion flame. The premixed combustible mixture is employed to minimize the inconsistency of the temperature field at the interface. The Cartesian grid used in numerical discrimination is 300 (uniformly distributed in axial direction) $\times$ 100 (expanded outward from the wall in normal direction). This grid configuration ensures 10 grids to cover each admission slot of fuel or oxidizer gases with spacing equal to 2 *mm* in the axial direction. The flow of gases inside the chamber is considered as a 2D, compressible, steady and laminar flow. The fuel is methane while the oxidizer is a pure air. Equivalence ratio of the premixed mixture is kept constant and equal to the unity. Combustion process is considered as described in equations (20-24) as a single-step kinetic reaction. Comparing the temperature contours inside the computational domain between the present model data and that of Chu and Yang (1996), a fair agreement is observed as shown in Fig. 11.

6 Results and discussions

In this study different parameters (turbulence intensity, chamber pressure, and the injected mass flux) that may affect the fuel concentration, reaction rate and the temperature inside the combustion chamber are studied. Moreover, the effect of

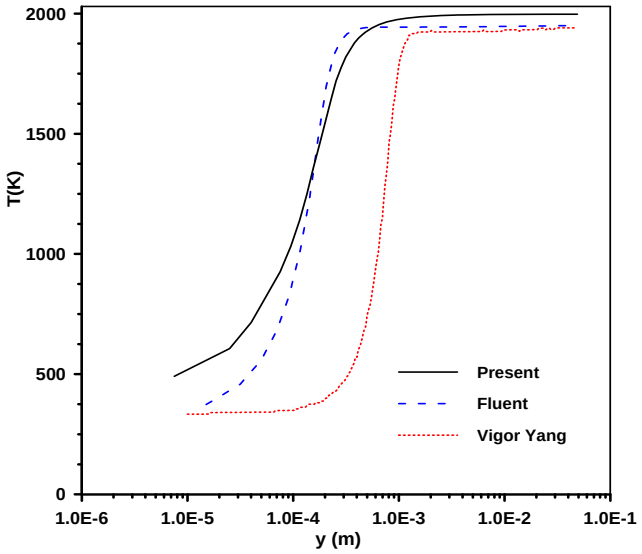

Figure 9: Temperature distribution in the normal direction inside the reaction zone of propane premixed flame. Comparison between the present model, Vigor Yang model [Tseng, Tseng, Chu and Yang (1994)] and Fluent code [Fluent 6.3 (2006)]

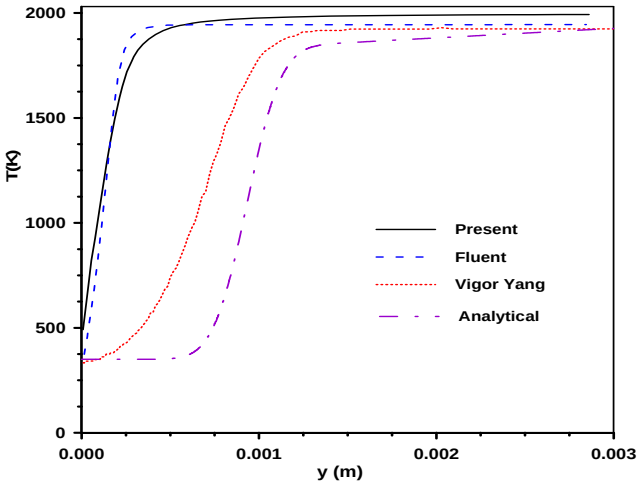

Figure 10: Temperature distribution in the normal direction inside the reaction zone of propane premixed flame. Comparison between the present model, Vigor Yang model [Tseng, Tseng, Chu and Yang (1994)] and Fluent code [Fluent 6.3 (2006)] as well as the analytical solution [Vyas, Majdalani and Yang (2003)]

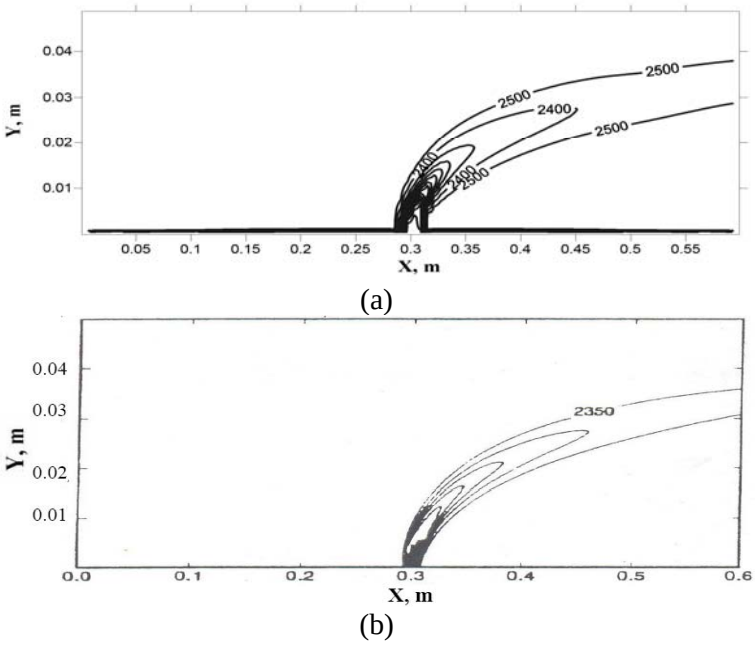

Figure 11: Temperature distribution in case of diffusion flame using the present model (a) and using the model of Chu and Yang (1996) (b)

nozzle existence at the end of the chamber on the combustion parameters is also introduced.

Figure 12 represents the effect of turbulence presence on the reaction process. It is found that a slight increase in the flame temperature that accompany with increase in reaction layer thickness as a result of slower reaction rate described in EBU model (equation 34). Data for the proposed test cases are listed in Table 2.

Table 2: Test cases examined in the present study

Mass Flux kg/m^2.s	Pressure (bar)	Turbulent intensity
0.2*	1*	0.001
0.4	5	0.01*
1.0	10	0.05
* Base case		

The effect of turbulence intensity on the fuel concentration is presented in Fig. 13. Since the great changes occur in the reaction zone above the sandwich model,

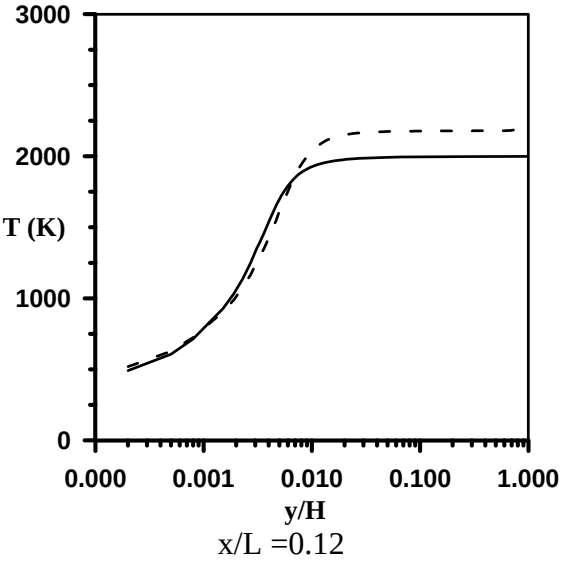

Figure 12: Comparison between temperature distribution in premixed combustion for laminar (continuous line) and turbulent cases (dashed line)

where the fuel and oxidizer introduced separately, than that above the premixed zone, the results are directed to capture the image above the former one. It is found that, increasing the initial turbulence intensity leads to raise the turbulence kinetic energy inside the flow field which in turn diffuses the reactants over a wide zone above the combustion surface. As a result the life time of fuel inside the reaction zone increases and gives the fuel the opportunity to penetrates deeply inside the combustion chamber. Moreover, this interesting behavior may contribute for another reaction away from the combustion surface if an oxidizer is found there. This trend reflects the behavior of the temperature contours as shown in Fig. 14. Temperature at low turbulence intensity exhibits more uniform distribution compared to the higher turbulence intensity, where the higher turbulence causes a stretching of the flame.

As the combustion process is governed mainly by reaction rate, Fig. 15 shows the following: At low turbulence intensity and according to the modified eddy breakup model, Arrhenius law becomes the governing and predominant factor. As a result, the reaction rate in this case becomes nearly temperature dependant. Moreover, it is found that the temperature increases downstream and, in turn, the reaction becomes faster. In case of increasing the turbulence intensity, the rate of fuel dissipation found to be the dominant factor and this behavior is seen clearly on the stretching

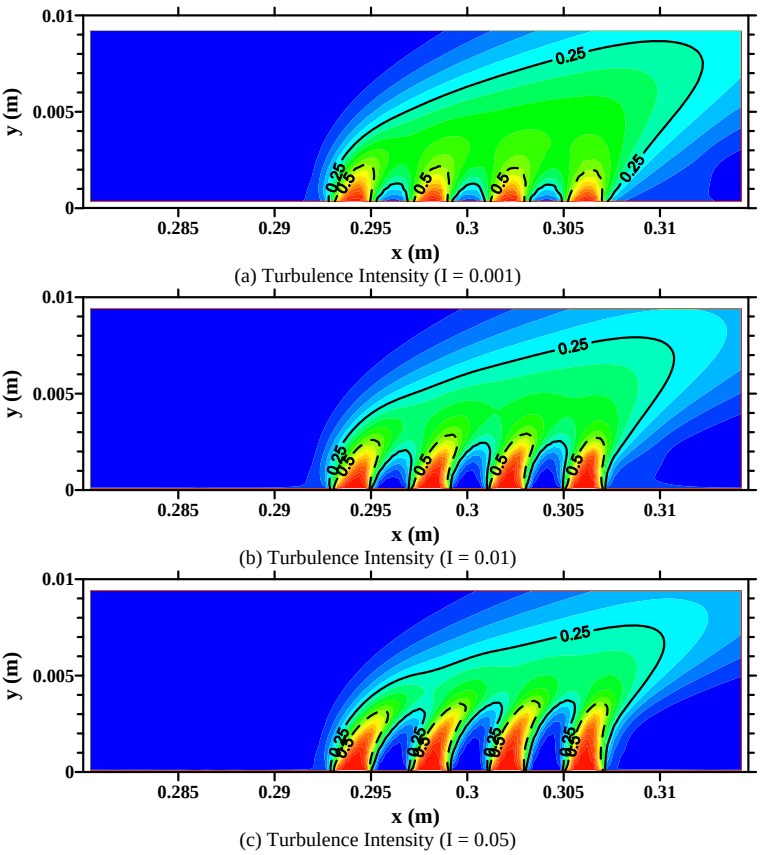

(a) Turbulence Intensity (I = 0.001)

(b) Turbulence Intensity (I = 0.01)

(c) Turbulence Intensity (I = 0.05)

Figure 13: Fuel concentration contours at different inlet turbulence intensities

of the flame downstream as shown in Fig. 15.

The second set of the results represent the effect of injected mass flux and the pressure inside the combustion chamber on the behavior of combustion process parameters inside the combustion chamber. Figure 16 shows the effect of increasing injected mass flux on the fuel concentration above the combustion surface and how penetrates across the chamber. It is found that, the increase in the injected mass flux from side wall, the vertical velocity component increases accordingly. Therefore, turbulence kinetic energy is increased causing a corresponding intense in turbulent diffusivity. Beside the resultant convective effect when increasing the injected mass flux, the flame lift off and consequently make the reaction zone to be wider than the lower injected mass flux as shown in Fig. 16. The figure shows also slight stretching in flame downstream. This can be attributed to the corresponding

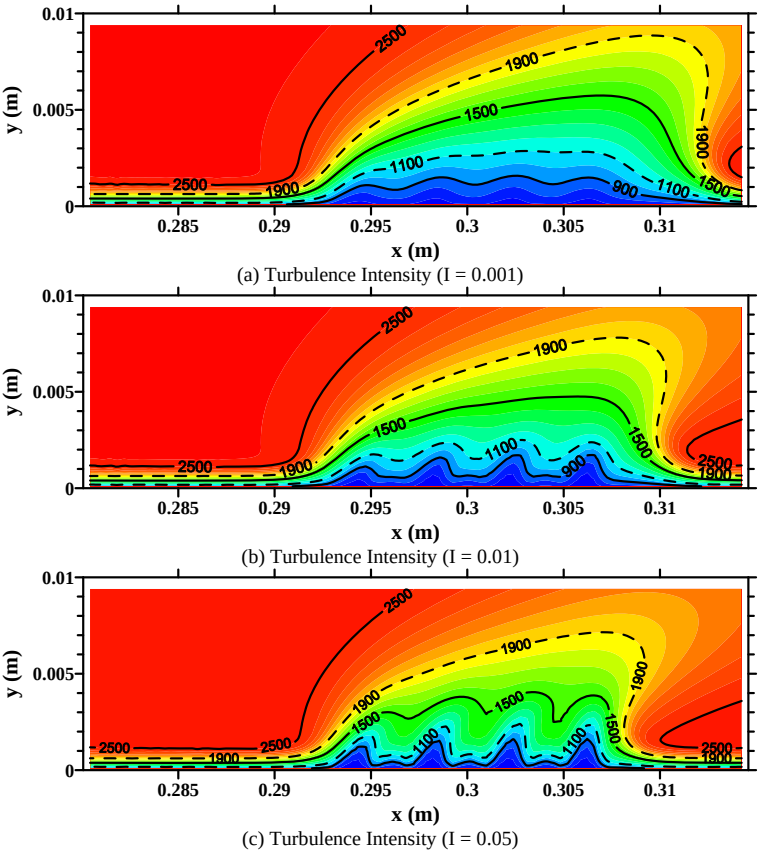

(a) Turbulence Intensity (I = 0.001)

(b) Turbulence Intensity (I = 0.01)

(c) Turbulence Intensity (I = 0.05)

Figure 14: Temperature contours at different inlet turbulence intensities

increase in vortex stretching downstream. The thicker reaction zone leads to lower fuel concentration gradient as shown in Fig. 17. Therefore, when increasing the mass flux, the heat released from reaction inside diffusion flame zone is distributed along deeper and thinner zone. This appears clearly from temperature contours as shown in Fig 18.

The effect of combustion chamber pressure on the fuel concentration, reaction rate and the temperature is presented in Figs. 19, 20, and 21. Pressure inside the combustion chamber is established as a result of gas production rate from combustion and discharge rate from the nozzle exit. The initial production of combustion gases subsequent to the ignition is greater than the rate of discharge. This contributes to increase the chamber pressure gradually, which is defined as the pressure rise period. By the end of this period, balance between the two rates exists and this keeps

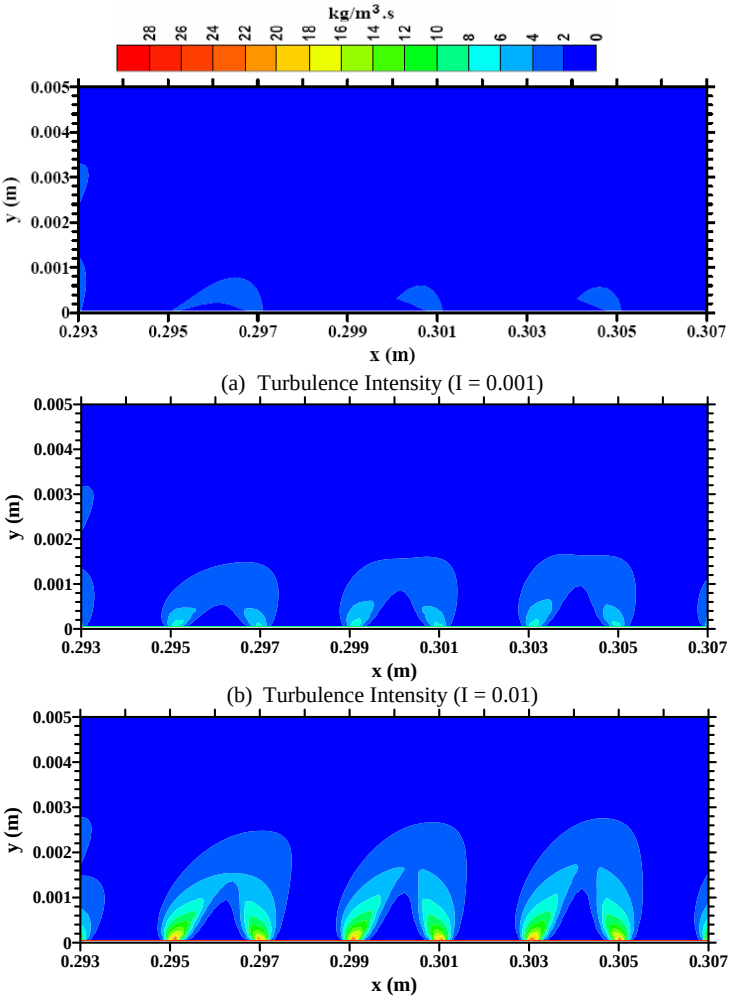

(a) Turbulence Intensity (I = 0.001)

(b) Turbulence Intensity (I = 0.01)

(c) Turbulence Intensity (I = 0.05)

Figure 15: Fuel reaction rate contours at different inlet turbulence intensities

the pressure at certain level called the operating pressure, until the end of the combustion process. The value of the operating pressure depends mainly on both the fuel factor and geometrical design considerations. When examining the effect of increasing the combustion chamber pressure on the combustion process, it is found that the gas density is increased as a result of increasing the combustion chamber pressure. For constant mass flux injected from the side wall, the relatively heavier gas has lower injection velocity. This in turn leads to reduce the flow field velocity

and its turbulent kinetic energy. Finally, the higher chamber pressure will reduce the turbulent diffusivity and leads to squeeze the reaction zone as shown clearly in Fig. 19. Consequently, higher fuel concentration gradient is obtained as shown in Fig. 20. As a result of faster consuming of fuel at higher pressure, temperature contours exhibits higher gradient in the vertical direction, while the temperature fluctuations at the fuel/oxygen interface is relatively diminished as shown in Fig. 21.

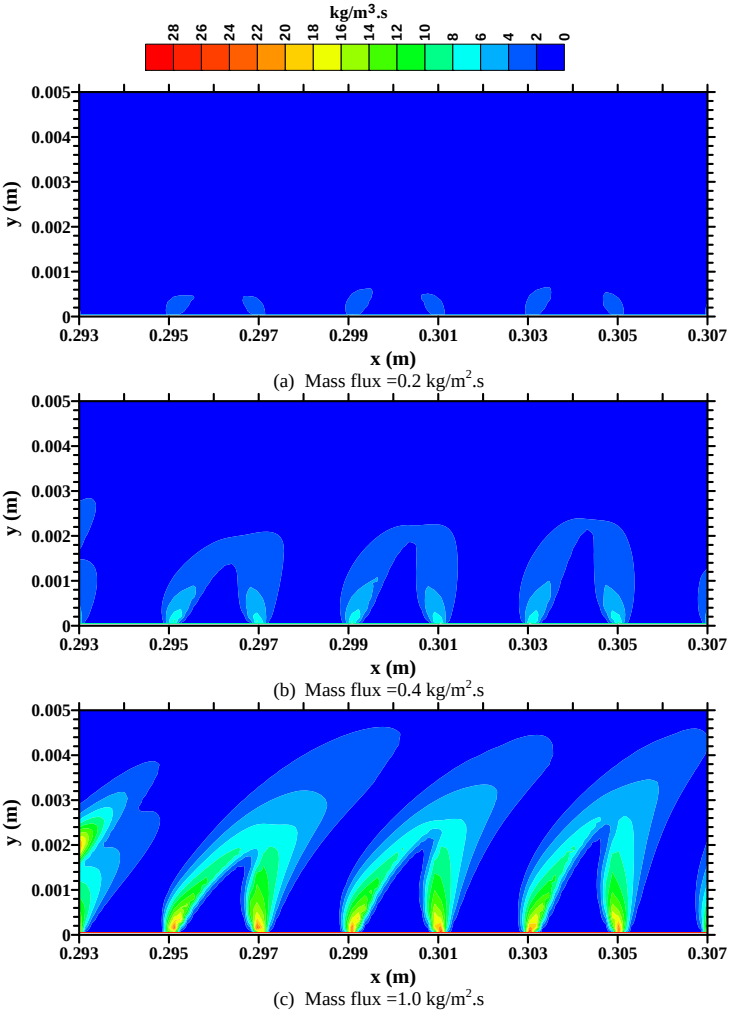

(a) Mass flux =0.2 kg/m^2.s

(b) Mass flux =0.4 kg/m^2.s

(c) Mass flux =1.0 kg/m^2.s

Figure 16: Fuel reaction rate contours at different mass fluxes

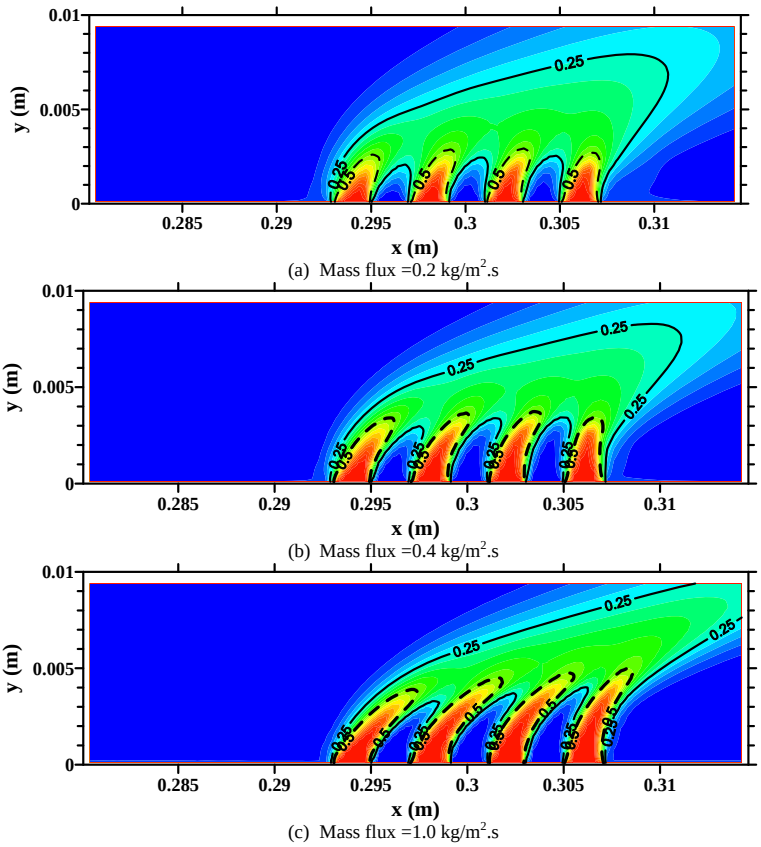

(a) Mass flux =0.2 kg/m^2.s

(b) Mass flux =0.4 kg/m^2.s

(c) Mass flux =1.0 kg/m^2.s

Figure 17: Fuel concentration contours at different mass fluxes

The last set of the results is considered in the present work when a nozzle is appended to the combustion chamber. The premixed combustion mode for the mixture injected perpendicularly to the side walls is employed. The base case illustrated in Table 2 is used as input data. The nozzle model used is a small scale two-dimensional convergent-divergent nozzle installed at the end of a chamber of length L=18 *cm* and half height H/2=5 *cm*. However, the dimensions considered here were not previously numerically or experimentally introduced and can be simply controlled according to the available one. The flow is generated as previously discussed due to a side-wall injection in the chamber and allowed to develop along the chamber before entering the nozzle, which freely discharges it to atmosphere. The nozzle has a throat area ratio $A_t/A_i = 0.389$, where A_t is the throat area and A_i is the duct cross-section area and an expansion ratio $A_e/A_t = 1.75$, where A_e is the

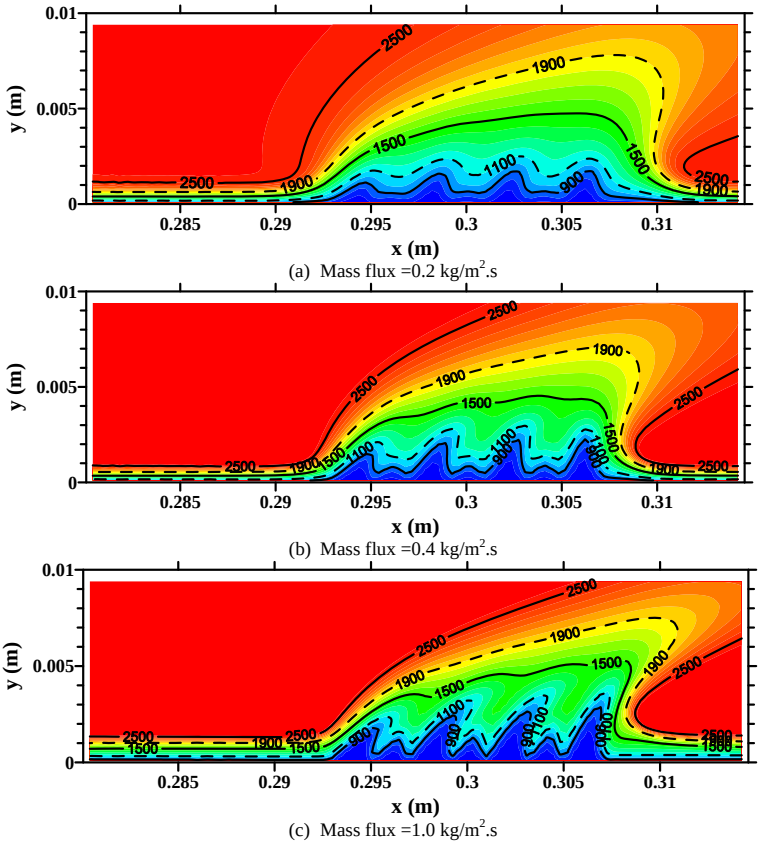

(a) Mass flux =0.2 kg/m^2.s

(b) Mass flux =0.4 kg/m^2.s

(c) Mass flux =1.0 kg/m^2.s

Figure 18: Temperature contours at different mass fluxes

exit area of the nozzle. The half-convergence and divergence angles of the nozzle wall read 20 and 10 degrees, respectively. The combustion products represented by carbon dioxide concentration along the entire physical domain are illustrated in Fig. 22. The figure shows high gradient inside very thin layer adjacent to the wall at which the combustion takes place. Beyond the flame edge, the products become in equilibrium state and no further change in concentration is obtained. With the progression of the products inside the nozzle and during the expansion process, velocity increases and corresponding stratification of products species takes place. When the mixture leaves the nozzle exit to the rear plenum, the concentration falls rapidly because of the mixing process with the fresh air. It is believed that the temperature attains maximum values in the chamber and gradually decreases as the axial distance increases downstream through the nozzle. In the other side, the fuel

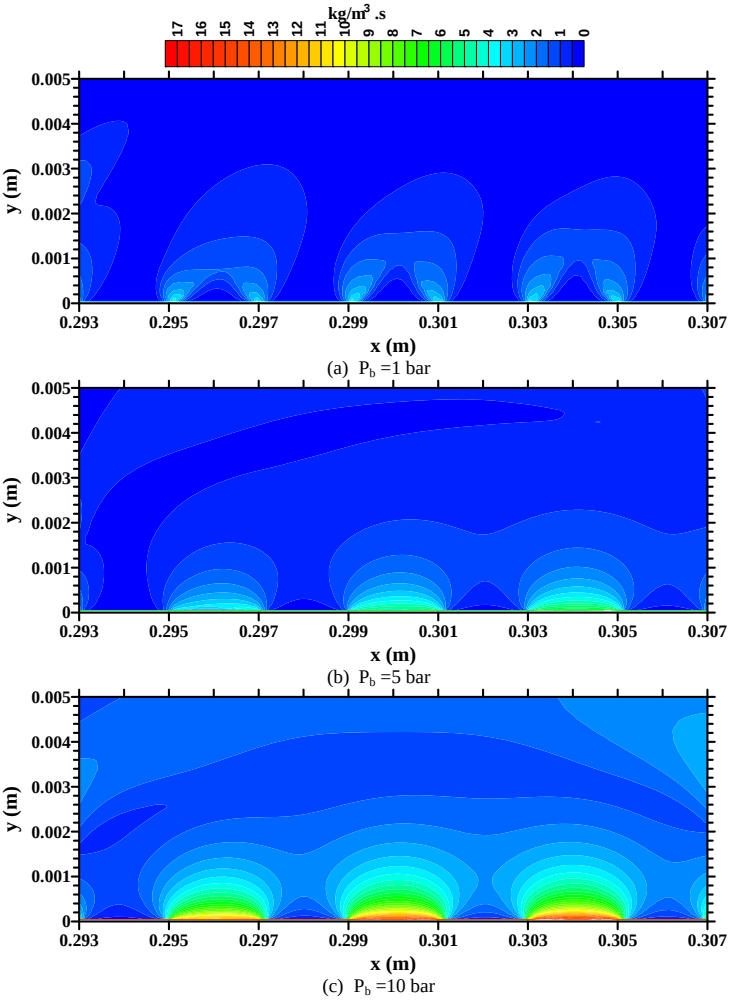

Figure 19: Fuel reaction rate contours at different back pressures

concentration inside the combustion chamber is found to be in a very narrow layer adjacent to the wall at which the fuel is consumed rapidly as illustrated in Fig. 23. The results show that the fuel is completely consumed in the combustion chamber and no fuel penetrates through the nozzle.

Finally, the numerical strategy used in this study accounted for the sandwich model for the diffusion flames and the mono-model for the premixed flames. This simulation represents the real life situation of the packed heterogeneous propellant. In spite of this modeling efforts for the injected fuel and oxidizer as gases give

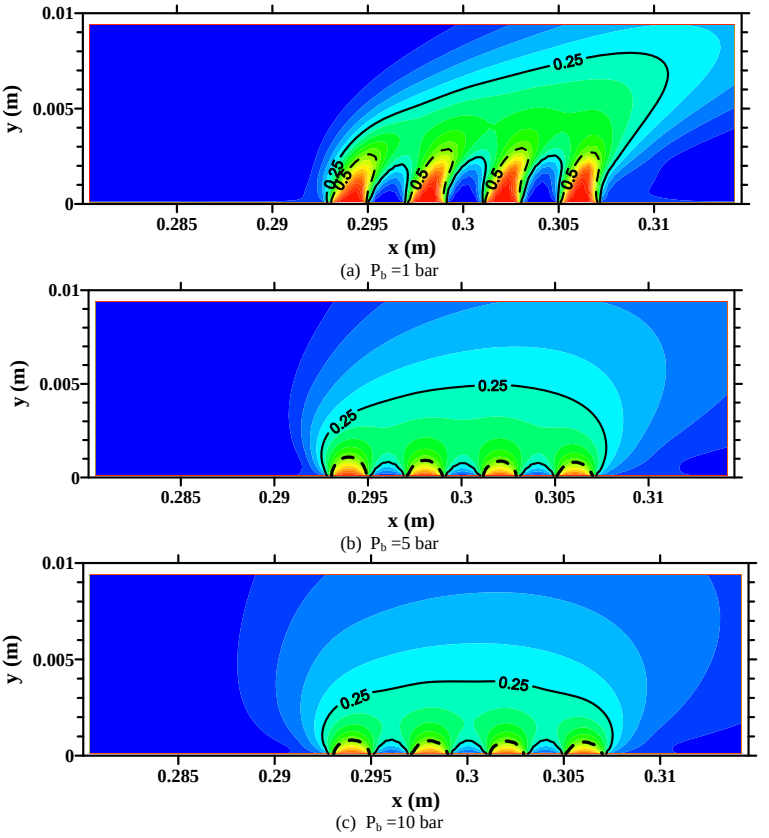

Figure 20: Fuel concentration contours at different back pressures

good insight about the nature of flow fields inside the combustion chamber, but don't reflect the philosophy of real solid propellant combustion in solid rocket motor. Anyway, the current modeling procedure will pave a road for more intensive computational work to the combustion of heterogeneous solid propellant, accounting for the turbulent, multi-dimensional gas phase physics, the solid phase physics and an unsteady non-planar description of the regressing propellant surface as extension to the laminar consideration by Hegab, Buckmaster, Jackson and Stewart (2000) and Hegab, Jackson, Buckmaster and Stewart (2001) and Hegab and Balabel (2007) for the long scale instead of the microscale modeling. Moreover, more intensive computational work is needed to study the effects of turbulent cross-flow in solid rocket motor chamber on the burning rate of a real long scale multimodal composite propellant instead of the cold one of Hegab and Kassoy (2006).

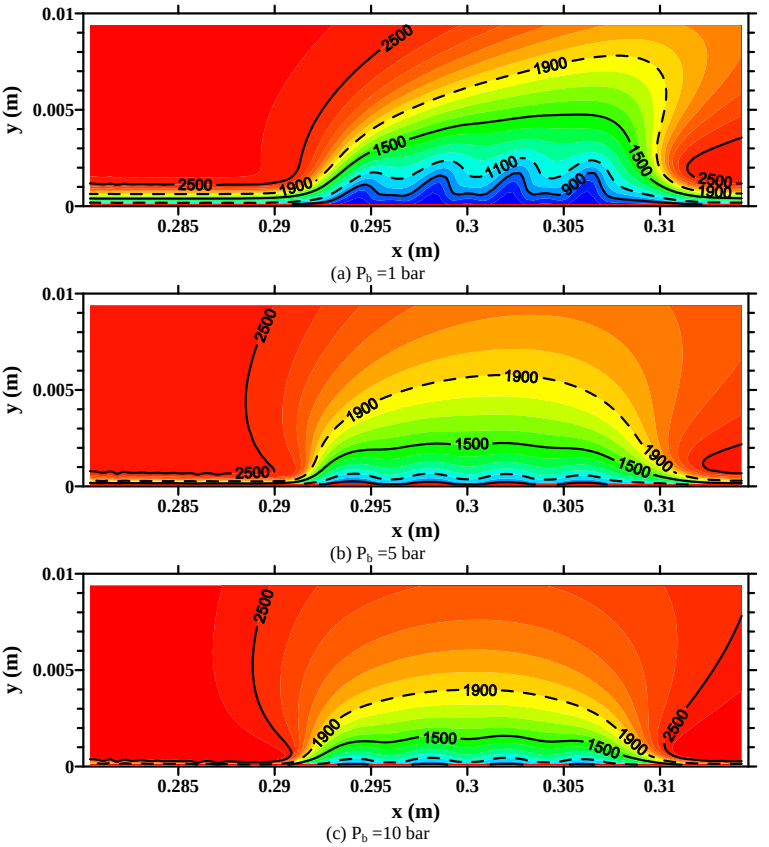

Figure 21: Temperature contours at different back pressures

7 Conclusion

In the current study, a comprehensive mathematical model is developed to simulate the turbulent combustion inside *SRM* combustion chamber. This model is based on solving strongly coupled set of partial differential equations representing the conservation of mass, momentum, species transport and energy as well as the two equations of turbulence. Eddy breakup model is used to account the effect of turbulence on the finite rate of reaction. The computational results of the model are compared with another data for different combustion modes with no nozzle. The comparison shows fair agreements. A further test of the cold model is introduced in a flow of convergent-divergent nozzle installed at the end of a straight duct in which the flow is injected from the side wall. The results are verified compared with available experimental data form literature.

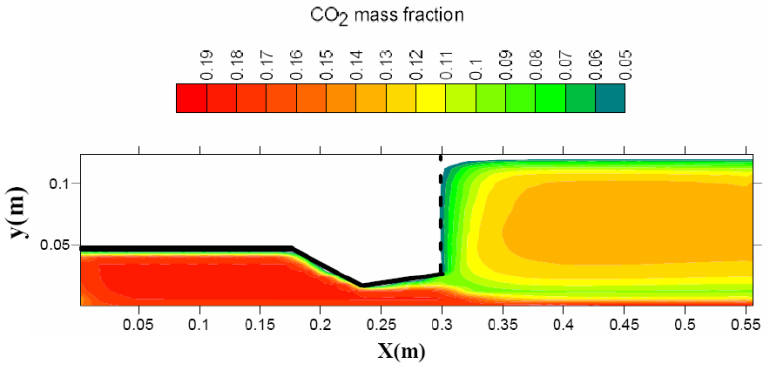

Figure 22: Variation of CO2 mass fraction inside a combustion chamber equipped with nozzle

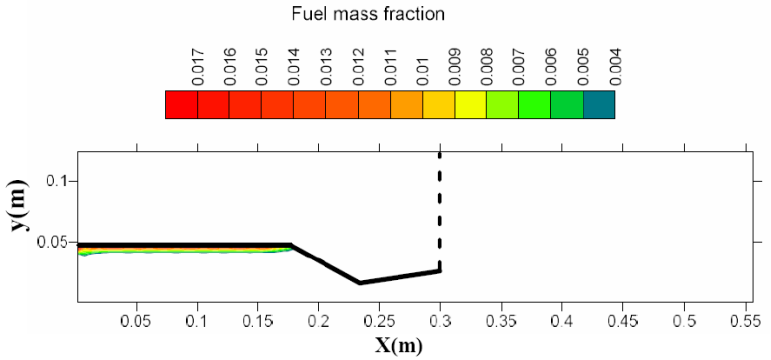

Figure 23: Variation of fuel mass fraction inside a combustion chamber equipped with nozzle

The model is then used and extended to study different cases of reactive flow to draw the following conclusion points:

- At low turbulence intensity, combustion is governed by Arrhenius law, while at high turbulence intensity; the rate of fuel dissipation becomes the dominant factor.
- Increasing the injected mass flux through side wall injection leads to the same combustion behavior at high turbulence intensity.
- When combustion occurs at high pressure, density will increase and this contributes for inhibiting the effect of turbulent diffusivity and squeezes the reaction zone.

- Moreover, the combustion parameters in case of nozzle existence are illustrated to capture full image about the reactive fluid dynamics behavior through the chamber, nozzle, and the rear plenum.

In general, the steady state combustion turbulent modeling gaves a good insight about the nature of the complex fluid flow in simulated solid rocket motor chamber, but doesn't reflect the perturbed generated combustion products of real composite propellant. As a result, more intensive computational work is aimed in the future to study the effects of turbulent oscillated cross-flow in solid rocket motor chamber on the burning rate of a real long scale multimodal composite propellant.

Acknowledgement: This work is supported by the Science and Technology Development Fund (STDF) through the project STDF-ID-108 (EGYPT).

References

Cherng, D. L., Yang, V., Kuo, K. K. (1989): Numerical study of turbulent reacting flows in solid propellant duct rocket combustors. *AIAA J. of Propulsion*, vol. 5, No. 6, pp. 678-685.

Chu, W. W.; Yang, V. (1996): Dynamic responses of diffusion flames to acoustic oscillations in a simulated solid rocket motor. *AIAA paper* 1996-0883.

Demirdzic, I.; Lilek, Z.; Peric, M. (1993): A Collocated finite volume method for predicting flows at all speeds. *International Journal for Numerical Methods in Fluids*, vol. 17, pp. 1029-1050.

El-Askary, W. A.; Balabel, A.; El-Behery, S.M.; Hegab, A. (2010): Prediction of turbulence transpiration resulting from asymmetric and symmetric mass injection in a porous channel. *ICFD10-EG-3070, Tenth International Congress of Fluid Dynamics*, December 16-19, 2010, Stella Di Mare Sea Club Hotel, Ain Soukhna, Red Sea, Egypt.

Fluent 6.3 manual (2006). Fluent Inc., Lebanon, USA.

Hegab, A.; Buckmaster, J.; Jackson, T.; Stewart, S. (2000): The Burning of periodic sandwich propellants. *AIAA Paper* 2000-3459, 36^{th}, AIAA/ASME/SAE/ASEE Joint Propulsion, July 17-19, Huntsville, Al., USA.

Hegab, A.; Jackson, T.; Buckmaster, J.; Stewart, D.; (2001): Non-steady burning of periodic sandwich propellants with complete coupling between the solid and gas phases. *Journal of Combustion and Flame*, vol. 125, pp. 1055-1070.

Hegab, A. M.; Kassoy, D. R. (2006): Internal flow temperature and vorticity dynamics due to transient mass addition. *AIAA Journal*, vol. 44, No. 4, pp. 812-826.

Hegab, A.; Balabel, A. (2007): Effect of ammonium perchlorate grain sizes on the

combustion of solid rocket propellant. *Proceeding of the 12-th Aerospace Science & Aviation Technology Conference*, (ASAT-12), 29-31 may, CHA-1, pp. 1-20, Military Technical College, Cairo, Egypt.

Heywood, J. P. (1986): Internal combustion engines fundamentals. McGraw Hill.

Lien, F. S.; Kalitzen, G. (2001): Computation of transonic flow with the $v^2 - f$ turbulence model. *International Journal of Heat and Fluid Flow*, vol. 22, pp. 53-61.

Mason, M. L.; Putnam, L. E.; Re, R. J. (1980): The effect of throat contouring on two-dimensional converging-diverging nozzles at static conditions. NASA Technical Paper 1704.

Srinivasan, R.; Reynolds, R.; Ball, I.; Berry, R.; Johnson, K.; Mongia, H. (1983):Aerothermal modeling program. NASA 84-12265.

Spalding, D. B. (1971): Mixing and chemical reaction in steady, confined turbulent flames. *13th Symposium on Combustion*, pp. 649-657.

Spalding, D. B. (1976): Development of eddy-breakup model of turbulent combustion. *16th Symposium on Combustion*, pp. 1657-1663.

Tseng, C. F.; Tseng, I. S.; Chu, W. W; Yang, V. (1994): Interactions between acoustic waves and premixed flamed in porous chambers. *AIAA paper* 1994-3328.

Versteeg, H. K.; Malalasekera, W. (2007): An introduction to computational fluid dynamics. Pearson Education, England.

Vyas, A. B; Majdalani, J; Yang, V. (2003): Estimation of laminar premixed flame temperature and velocity in injection driven combustion chambers. *Combustion and Flame*, vol. 133, pp. 371-374.

Westbrook, C. K.; Dryer F. L. (1981): Simplified reaction mechanisms for oxidation of hydrocarbon fuels in flames. *Combustion Science and Technology*, vol. 27, pp. 31-43.